Applied Geochemistry 118 (2020) 104624

Contents lists available at ScienceDirect

Applied Geochemistry

journal homepage: http://www.elsevier.com/locate/apgeochem

Concrete perturbation in a 13-year in situ concrete/bentonite interaction from FEBEX experiments. New insight of 2:1 Mg phyllosilicate precipitation at the interface

Stephane Gaboreau [a], Enrique Rodríguez-Cañas [b], Urs Maeder [c], Andreas Jenni [c], Maria Jesús Turrero [d], Jaime Cuevas [e,*]

[a] BRGM, Environment and Process Division, Avenue Claude Guillemin, F-45060, Orléans Cedex, France
[b] IDiBE. Universidad Miguel Hernández (UMH), 03202, Elche, Alicante, Spain
[c] RWI, Institute of Geological Sciences, University of Bern, Baltzerstrasse 3, CH-3012, Bern, Switzerland
[d] Unidad de Geología Ambiental, Departamento de Medio Ambiente, CIEMAT, Av. Complutense 40, 28040, Madrid, Spain
[e] Departamento de Geología y Geoquímica. F. Ciencias. Universidad Autónoma de Madrid, 28049, Madrid, Spain

ARTICLE INFO

Keywords:
Deep geological repositories
Geochemical alteration
Porosity
Cement
Clay
Bentonite

ABSTRACT

The Engineered Barrier System (EBS) implemented in full-scale experiments are designed to provide an understanding of the long-term performance of Deep Geological Repositories (DGR) as nuclear waste repositories. The existing interfaces between the engineered barrier materials, such as concrete and bentonite, constitute reactive surfaces on which the thickness and intensity of degradation of the material, which may affect the confinement properties, are under investigation. This study focuses on a concrete projected on a saturated compacted bentonite from the in situ FEBEX experiment, emplaced in the Grimsel Test Site (GTS, Switzerland) and dismantled during 2015 after 13 years of functioning.

Preserved sections crossing the interface have shown macroscopic heterogeneities in 1–2 cm of the shotcrete from the contact with bentonite that presumably affected the porosity distribution. In this area, the distribution of mineral and chemical components has been analyzed in detail, both in concrete that is distant from the interface and in contact with the bentonite.

The information provided by detailed mineralogical mappings was consistent with quantitative chemical analysis. Chemical mappings are used to explain the distribution, nature and evolution of the phases in the concrete at the interface with clay. The role of porosity, presumably affected by the initial application of the shotcrete, has influenced the characteristic geochemical reactions in the bentonite-concrete interaction. The chemical composition of di- and tri-octahedral Al–Mg smectites, in the mixing trend of high-charge beidellite-saponite, were identified in the concrete in the degraded area at the interface.

1. Introduction

Deep Geological Repositories (DGR) are currently the most acceptable solution for safe long-term storage of high-level radioactive waste (HLRW) (Chapman, 2019). The waste is thus isolated from the biosphere by a system of engineered and natural barriers. The Engineered Barrier System (EBS) usually consists of a metal sleeve surrounding the waste, forming a canister cylinder, followed by a compacted bentonite clay barrier. The host rock, in which access galleries are excavated, will need concrete vaults to support the walls (clay rocks) or concrete plugs (crystalline rocks) to seal and stop the swelling of the hydrated bentonite backfill inside the gallery. Increased confidence in DGR could be achieved based on the detailed multi-scale analysis and characterization carried out after the dismantling of long-term (10–30 years) in situ simulated experiments.

The concrete-clayrock/bentonite interface is considered as one of the most reactive interfaces in the EBS system. Due to the large geochemical contrasts between concrete (pH ~13) and clays (pH ~7), chemical reactions are expected to induce modifications in both the chemical and physical properties of clayey and cementitious materials. These highly contrasted pH and Eh conditions will lead to ion diffusion. A series of reactions are likely to occur, such as ion exchange on the clay minerals'

* Corresponding author.
E-mail address: jaime.cuevas@uam.es (J. Cuevas).

https://doi.org/10.1016/j.apgeochem.2020.104624
Received 14 October 2019; Received in revised form 24 March 2020; Accepted 27 April 2020
Available online 11 May 2020

surface, dissolution of some minerals, and precipitation of secondary phases at the interfaces. In addition, these reactions will change the pore network and therefore the hydraulic properties of both the clay and the cementitious materials (Chagneau et al., 2015; Xie et al., 2015). The difference in the pore water pH in both materials is ruled by the equilibrium of the assemblage of solid phases. The pH of ordinary Portland cement (OPC) concrete equilibrates at pH 13–12 (Bullard et al., 2011), and clay or bentonite at 7–8 (Fernández et al., 2004; Turrero et al., 2006). While clay tends to be stable in the long-term (Bildstein and Claret, 2015), concrete materials are subject to continuous evolution by means of groundwater or clay pore water hydrating and dissolving the major cement phases. In response to the progressive degradation of the cementitious materials, the pH of the pore water in cement is controlled by the solubility of portlandite ($Ca(OH)_2$) and later the dissolution of calcium silicate hydrates (C–S–H) with variable Ca/Si from high (1.6–1.2) to low ratio (1.0–0.7). Calcite also precipitates in replacement of cement phases, in as far as soluble inorganic carbon species are present in the bentonite or clay pore water environments (Glasser and Matschei, 2007). The pH gradient produces an alkaline front with the capacity to partially alter the mineralogy in both the clay and the concrete (Dauzeres et al., 2014, 2016; Gaboreau et al., 2011, 2012; Jenni et al., 2014). The intensity and propagation of these reactions depend on the type of cement and clay materials, the available pore volume and the efficiency and magnitude of water and solute transport.

One of the most recognized dissolution/precipitation reactions at these cementitious materials-clay interfaces is the precipitation of Mg-silicate hydrates (M-S-H), described as Mg-perturbation (Bildstein and Claret, 2015; Lerouge et al., 2016). It is a common place representing the result of the reactive transport processes caused by the chemical gradients in clay/cementitious materials (Dauzeres et al., 2014; Fernández et al., 2018b; Lerouge et al., 2017). The increase in Mg concentration is usually characterized, either in the concrete (Jenni et al., 2014; Lerouge et al., 2017), both in cementitious materials and bentonite (Fernández et al., 2017), or just in the clay, sometimes several mm from the interface in clay rocks (Mäder et al., 2017).

The release of dissolved Mg in clay pore water may originate from cation exchange from the bentonite exchange complex, through the dissolution of Mg minerals in the clay rocks (i.e. dolomite) or the dissolution of Mg phases in the cementitious materials. At low temperature in alkaline conditions at pH $>$ 10.5, brucite precipitates (Pokrovsky and Schott, 2004). At relatively lower pH values of 10–9, Mg silicates such as saponite, and Ca and Mg di-trioctahedral smectites are predicted to precipitate (Marty et al., 2014) and have been characterized in clay-concrete interactions (Lerouge et al., 2017). The nature of these neogenic M-S-H phases in concrete materials reveals similar structural properties to that of 2:1 and 1:1 magnesium layer phyllosilicates (Nied et al., 2016; Roosz et al., 2015; Vespa et al., 2018). Those precipitated in clay or bentonite are very difficult to characterize because they are mixed with the present assemblage of phyllosilicates. Nevertheless, what is known from their synthesis in the laboratory is that they have a very limited capacity to form solid solutions with C–S–H phases and precipitate as separate phases, containing very small amounts of Ca (Bernard et al., 2018a, 2018b; Lothenbach et al., 2015).

The FEBEX project (Full-scale Engineered Barriers Experiment in crystalline host rock) was one of the experiments implemented in the Underground Research Laboratory (URL) located at the Grimsel Test Site in Switzerland. It was based on the Spanish reference concept for disposal of HLRW in crystalline rock (AGP Granito: Huertas et al. (2006)). The present article focuses on the characterization of a 13-year (2002–2015) concrete-bentonite interface from this experiment. The concrete plug placed to retain the bentonite swelling in the in situ GTS gallery represents an ideal heterogeneous interface for analyzing the microstructural aspects of a real EBS. This document intends to show an example of the chemical evolution at the interface between concrete and bentonite, in a real case of gallery sealing with the heterogeneities that could be induced by the man-made set up. The evolution of the concrete phases in contact with clay materials and the porosity distribution will be analyzed in regard to the characteristics of shotcrete. The present study is part of a global and exhaustive characterization work performed on the FEBEX project (FEBEX-dp (http://www.grimsel.com/gts-phase-vi/febex-dp/febex-dp-introduction). This study comes under the European project CEBAMA (https://www.cebama.eu/) which attempts to describe the microstructural and geochemical perturbation of some engineered cement-based materials.

The paper attempts to show in detail microstructural and mineralogical evolution at the interface between concrete and bentonite, revealed by porosity and mineralogical mapping methodologies described by (Gaboreau et al., 2012; Gaboreau et al., 2017; Gaboreau et al. (2011)). The alteration of the hydrated cement phases and the characteristic of the formation of neogenic phase at the concrete-bentonite interface are described within the microstructural framework acquired by electron microscopy, quantitative electron probe microanalysis (EPMA) and quantitative porosity mapping.

2. Materials and methods

2.1. In situ bentonite/concrete interface

The studied material is part of the FEBEX in situ experiment. The FEBEX project simulated the waste canisters that are placed horizontally in drifts and surrounded by a clay barrier constructed from highly compacted bentonite blocks (ENRESA, 1995). Two cylinder heaters were maintained at a constant temperature of 100 °C on their surface, facing an annulus of compacted bentonite that filled the gap up to the granitic wall. A concrete plug was applied to seal the drift end. The operational phase started in 1997. In 2002, after five years of operation, one of the heaters was switched off and dismantled, along with the surrounding bentonite. A concrete plug was made by shotcrete technology to seal the remaining part of the experiment. The experiment was definitively dismantled in 2015.

A piece of compacted FEBEX bentonite/concrete preserved from the dismantling of the FEBEX project (Cloet and Turrero, 2019) is the focus of this paper. The sample was labeled as C–C-32-6-OC-cb-III and is one of the three unaltered bentonite/concrete contacts that were obtained by a special overcoring technique (Jenni et al., 2014; Mäder et al., 2016).

The FEBEX bentonite was extracted from the Cortijo de Archidona deposit (Almería, Spain), (Caballero et al., 2005). The montmorillonite content of the FEBEX bentonite is above 90 wt% (92 $\pm$ 3%) and contains variable quantities of quartz (2 $\pm$ 1 wt%), plagioclase (3 $\pm$ 1 wt%), K-feldspar (traces), calcite (1 $\pm$ 0.5 wt%), and cristobalite-trydimite (2 $\pm$ 1 wt%) (ENRESA, 2006; Ramirez et al., 2002). Bentonite was used to form compacted bentonite blocks, at a dry density of 1.7 g/cm^3. They were installed around the cylinder heaters and in the gaps in the gallery. The obtained dry density, considering the heterogeneities and the accommodation of the bentonite blocks within the gaps, is 1.5–1.6 depending on the geometry of the experiment and the proximity of the granite walls and the heater respectively (Villar, 2017).

The composition of the shotcreted plug was: CEM II A-L 32.5R paste (430 kg/m^3), water (170 kg/m^3), nanosilica (30 kg/m^3), aggregates 0–8 mm (1700 kg/m^3), steel fibers (50 kg/m^3), polypropylene fibers (800 g/m^3), poly-carboxylate superplasticizer GLENIUM T803™ (1.5%), a liquid curing compound MEYCO TCC 735™ (1%) and accelerant MEYCO SA 160 E (6%, $Al_2(SO_4)_3$ based) (Huertas et al., 2006).

The first layer of the shotcrete (up to 2 cm thickness) was projected with a water/cement ratio of the fresh gunite that was considered too high (0.6), so it rebounded and only a gunite layer of about 2 cm could be made. After reforming this mix with a higher proportion of accelerant compound (up to 8%), the other layers were made thicker to give a total average thickness of about 95 cm. The photographs of the preserved interfaces shown in Fig. 1 capture the distinct texture of the initially projected 2 cm band.

The bulk mineralogy of the concrete consists of quartz (40-30 wt%),

calcite (30-20 wt%), plagioclase (albite, 15-10 wt%), orthoclase (10-5%), ettringite (10-5%) and portlandite, biotite, muscovite, and clinochlore (<5%). The mineralogy is complex and it is not possible to ascertain the contents of anhydrous cement phases or hydrates such as calcium silicate hydrates (C–S–H). The mineralogy has been analyzed by a semi-quantitative reference intensity ratio (RIR) based method as reported in Cloet and Turrero (2019).

2.2. Quantitative porosity mapping

Spatialized quantitative porosity mappings were obtained from autoradiography using the method developed by Pret (2003) for clay materials. This method has previously been applied and proven on other cement-clay interfaces (Gaboreau et al., 2011, 2012; Lerouge et al., 2017). Impregnation conditions were adapted to the cementitious materials and were chosen according to the drying recommendation of Gallé (2001), which showed the impact of drying on cementitious materials. The sample was oven-dried for 20 days at 70 °C under vacuum. The sample was then impregnated through diffusion for 90 days with ^{14}C Methylmethacrylate (MMA) with a tracer activity of 10 μCi/mL. The polymerization was induced by gamma irradiation with a total dose of 120 kGy. The textural state of the impregnated sample is expected to be close to the textural state encountered for samples in equilibrium with water in response to the resin properties, viscosity and dipole moment that are close to those of water (Massat et al., 2016; Pret et al., 2010a), implying that interlayer space is impregnated.

Two polished sections were prepared with a low speed diamond saw by cutting the sample in half. They were polished using diamond powders with grain size down to 0.05 μm. The thick sections were then exposed on Kodak Biomax MR film for 4 days. Exposure times were optimized according to the varying bentonite and cementitious material porosities to acquire the best porosity contrast. The autoradiographs were then digitized in 8-bit images with a resolution of 2400 dpi (10.4 × 10.4 μm^2 pixel size). The local blackening of the film (expressed by a local optical density) is proportional to the local concentration of radioactive resin. A set of standards of known activity were simultaneously exposed on the autoradiograph films to obtain the relationship between the local activities and optical densities. The experimental data were fitted using the calibration function proposed by Hellmuth et al. (1993). A local mean porosity was then calculated for each pixel of the digitized autoradiograph from the calibration function and tracer activity using the relationships provided by (Sammartino et al., 2002) and in house autoradio software (Pret, 2003). Local pixel porosities include the connected micro-, meso-, and macro-porosity. For each autoradiograph, a combination of analysis methods was used to reveal the porosity distribution. Porosity frequency histograms were computed on different sub-areas of the autoradiograph by counting the number of pixels with similar porosity values. To localize the spatial heterogeneities, porosity maps were then computed by displaying the local porosity of each pixel using a linear gray level scale ranging between two porosity values identified on the histogram. Porosity profiles were computed to reveal changes in porosity as a function of two distal points. Profiles were calculated for one pixel along a straight line (1 pixel width) or dilating the straight line by a given number of pixels in width to reach average porosities with improved statistical error.

2.3. Qualitative chemical maps

The polished but uncoated sample surface was examined in an electron microscope (Zeiss EVO-50 XVP) equipped with a backscattered electron (BSE) detector and an EDAX Sapphire light element detector in low vacuum mode (10 Pa) at a beam acceleration of 20 keV and a working distance of 8.6 mm. The beam current was adjusted to yield a dead time of 10–20% for Energy-Dispersive X-ray spectroscopy (EDX). EDX element maps with a resolution of 3 μm/pixel were acquired using a dwell time of 400 μs, repeating 64 frames. The total measuring area was divided into fields of 733 × 573 μm that were merged after acquisition. Normalization of each field to total counts was necessary to compensate for filament weakening, which was significant throughout the total measurement time of approximately 50 h.

The merged EDX element maps covering an area of 33.0 × 1.7 mm were further analyzed using the software ImageJ combined with a suite of in-house developed image analysis routines. The porosity above 3 μm in size, all aggregates in the shotcrete, and also accessory minerals were

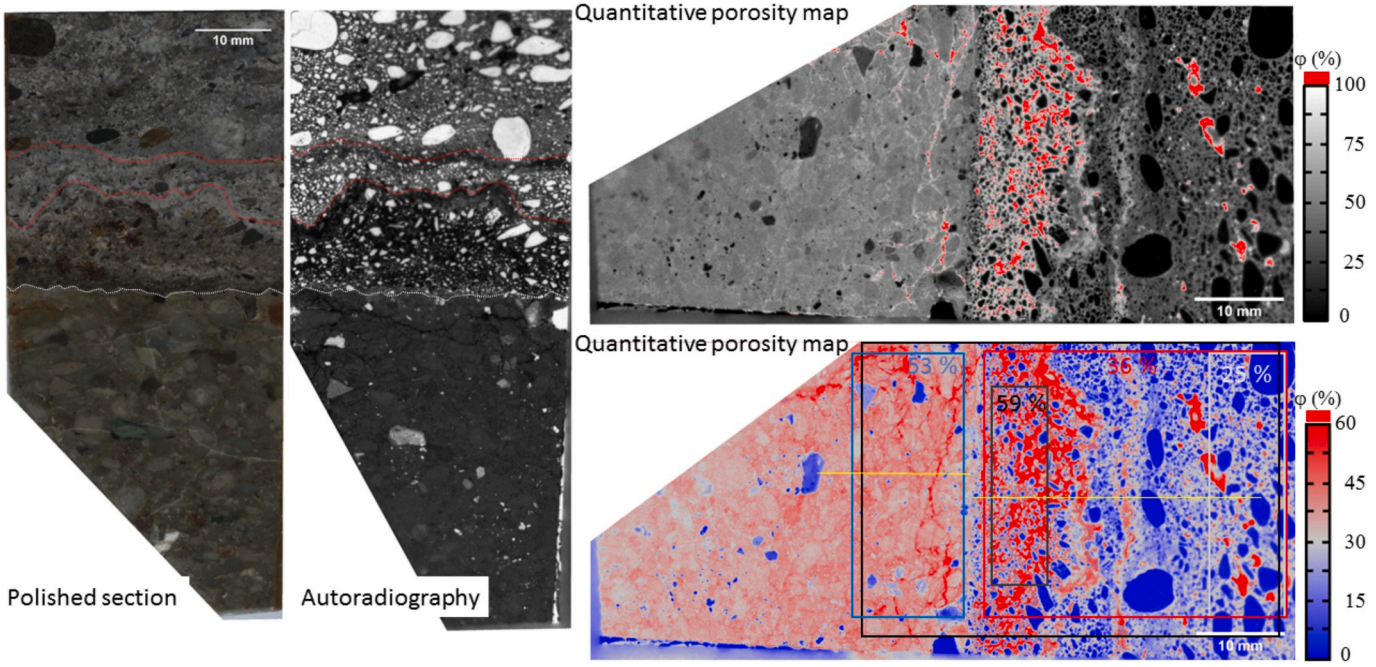

Fig. 1. Bentonite/concrete polished section, autoradiography and corresponding quantitative porosity maps displayed in gray values and false color. The colored squares and lines represent the different measurements (Porosity profiles, porosity histogram and total connected porosity) performed on the autoradiography. (For interpretation of the references to color in this figure legend, the reader is referred to the Web version of this article.)

segmented. EDX counts of layers parallel to the irregular interface with a thickness of 3 μm in cement and bentonite were summed. Counts from porosity, aggregates, or accessory minerals were discarded based on the segmented images. The average counts per pixel of each layer, originating from the cement or bentonite matrix, were plotted as a function of the distance from the interface to characterize zonation. The matrices also include porosity, accessory minerals or neo-formations smaller than approximately 3 μm that could not be reliably segmented at the chosen resolution.

2.4. Quantitative chemical maps

Quantitative X-ray intensity maps and a BSE image (Fig. 1) were acquired with a Cameca SX *Five* EPMA equipped with five wavelength dispersive spectrometers (WDS) and operating at 15 keV and 30 nA. To investigate the distribution of the ten major elements identified in the concrete (Si, Ca, Al, Mg, Fe, Na, K, Ca, S, Cl), the area was scanned twice, because the number of simultaneously detected elements was constrained by the number of available spectrometers. Kα peak intensities were collected using large LTAP (Large Thallium Acid Phthalate), LPET (Large Pentaerythritol, PET (Pentaerythritol), TAP (Thallium Acid Phthalate) and LiF (Lithium Fluoride) monochromator crystals, allowing for a high counting rate and short dwell time (~4 s) for a quantitative point analysis. This dwell time is too time-consuming for mapping mode, so a shorter counting time of 100 ms per pixel was used, as discussed in (Pret et al., 2010b). After the acquisition, no evidence of beam damage was identified in the mapped area. To reduce the total acquisition time (two days), the background with subtraction of X-ray emission peaks was not measured, since its contribution at short dwell times and for major concentrations is low (Goldstein et al., 1992), and as recording it would have doubled the acquisition time. A standard-based PHIRHOZ matrix correction (Merlet, 1994) was then applied to provide a weight percentage for each element per pixel. The 512 x 512 pixel elemental maps were recorded by stage rastering using a stationary beam, with a spatial resolution of 2 μm per pixel.

2.5. Quantitative mineral maps

Mineralogical maps were created to display the spatial distribution of the minerals over a surface area of 1×1 mm^2 with resolution of 2 μm following the methodology developed by (Gaboreau et al., 2017) and using the μMAPphase software (Pret et al., 2010b). This methodology consists in identifying the mineral phases composing the analyzed area from step by step projections of the scanned elemental composition points, and converting them into ternary plots from which contrasting chemical compositions for all the solid phases can be visualized.

All the pre-processing steps for converting the initial quantitative X-ray maps given in element weight percent (At_i wt%) into element molar percent (At_i mol%) have been described in (Pret et al., 2010b). This conversion led to a chemical oxide composition for each pixel of the map. All the pixels of the mapped area were plotted in ternary diagrams, in which each axis of the plot represents the concentration of an element or a combination of elements. This method was not affected by porosity variations as normalized axis weights were used to generate the ternary scatter plots.

Pixels with similar chemical compositions (i.e. a cluster) in the ternary diagrams were selected with a polygon tool and back-projected on a mineral map using the same color as the selected polygon. This method of segmentation based on ternary diagrams was particularly efficient for locating small crystals and mineral mixtures (Gaboreau et al., 2017; Pret et al., 2010b). For our study, another advantage of this method was the possibility of comparing the chemistry of the two mapped areas based on the position of the clusters in the projections. For most materials, the projection using only three elements was not sufficient to distinguish all the mineral phases, so we used a succession of ternary diagrams in which the axes covered a large range of element combinations. The theoretical compositions of the main clinker phases, pozzolans, hydrates and aggregates were superimposed on each of these diagrams in order to facilitate reading and interpretation of these chemical scatterplots.

3. Results

3.1. Quantitative porosity mapping by autoradiography

An impregnated ^{14}C-PMMA polished section of the bentonite/concrete interface is presented in Fig. 1. The sample size is 4×8 cm and it displays a dark green bentonite and a gray concrete. Some grains/aggregates are apparent over the bentonite surface while some optical heterogeneities are observable in the concrete at the interface, enhanced with the dotted red lines (Fig. 1). The autoradiography reveals that these color contrasts in the concrete correspond to porosity heterogeneities. Autoradiography also allows the distribution of non-porous aggregates to be visualized. They appear in white in the concrete, with no coarse grains in the first 2 cm in contact with the bentonite. The spatial heterogeneity of the porosity can be visualized by displaying, on the calculated porosity map, the porosity value measured for each pixel using a linear gray scale or false color (Fig. 1). We note that the gray and false color scales chosen for encoding the two porosity maps are different to maximize the visual contrast between bentonite and concrete. The total mean porosity is calculated over surface areas plotted on the porosity maps (Fig. 1). In the concrete, the porosity map reveals two areas with different porosities. At the interface, the total connected mean porosity of the concrete is 59% while a few centimeters from the interface the porosity decreases down to 25%. In the bentonite, no strong evolution of the porosity is depicted. The distribution of the porosity reveals heterogeneities, with low porous aggregates in between higher porosities. The total mean porosity is 53%. The frequency histograms of porosity distribution, corresponding to the area plotted on the porosity maps, were calculated for the whole autoradiography, the concrete and the bentonite surfaces (Fig. 2). The different histograms are superimposed on Fig. 2.

The porosity histogram of all the surfaces displays different modes centered on 0%, 30% and 50%. The different modes correspond to the porosity of each material. The FEBEX bentonite has a roughly Gaussian distribution with a maximum intensity at 55% and a small contribution centered on 30%, indicating a bimodal distribution with the presence of agglomerated bentonite surrounded by less dense bentonite. Some non-porous grains are quantified with a distribution centered on 0%. The porosity distribution of concrete is more complex with two main modes centered on 0 and 30% and spreading up to 100%. These distributions indicate a multi-component assemblage. Distributions were discriminated by plotting histograms from areas at the interface (mean porosity of 59%) and centimeters from the interface (mean porosity of 25%). The superimposition of these three histograms (Fig. 2) shows that the contribution centered on 0% corresponds to the non-porous aggregates of the concrete identified in the three areas. The mode ranging from 20 to 50% indicates the porosity value of the cement binder in the concrete at the interface. At the interface, the porosity of the cement binder increases up to 70–80%. The value at 100% is for macropores filled with pure 14-C PMMA.

In order to analyze the extent of perturbation in terms of porosity evolution, porosity profiles were computed through the bentonite and the concrete up to the interface (yellow lines, Fig. 1). The evolution of the porosity in the bentonite and concrete are given in Fig. 3, over profiles 500 pixels wide (i.e. 5 mm wide), mimicking the size of subsamples usually used for bulk measurements. The same profiles were computed with a width of 10 pixels (i.e. 100 μm wide). The 500 pixel-wide profile displays a slight increase in porosity in the direction of the interface. An increase in higher porosities in the last 5 mm before the interface can be noted, explained by the presence of cracks (pure red on porosity map, Fig. 1). Along the 10 pixel-wide profile, the evolution of

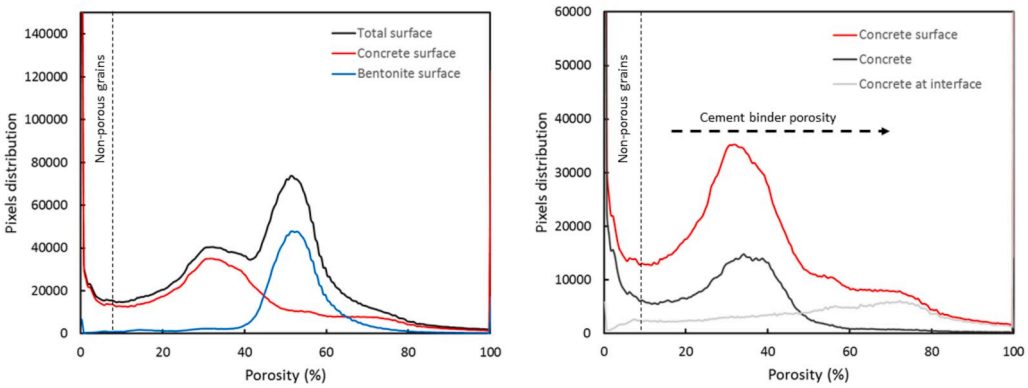

Fig. 2. Porosity frequency histograms of the total surface, concrete surface and bentonite surface (left); Porosity frequency histograms of the concrete surface, concrete at the interface and concrete distant from the interface (right). For the exact position of the plotted areas, refer to Fig. 1.

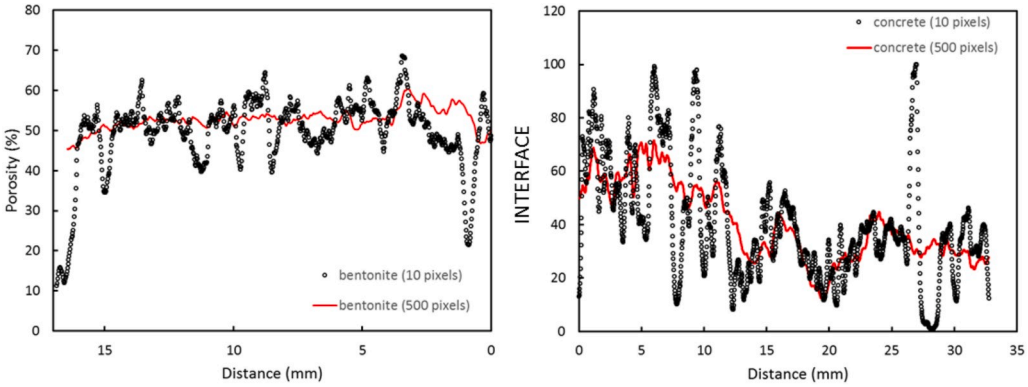

Fig. 3. Total connected porosity profiles from autoradiography. On the left side, the porosity of the bentonite is represented and on the right that of the concrete. Profiles are given with an integration of 10 and 500 pixels in the bentonite and concrete.

the bentonite porosity is like a roller coaster with an alternating pattern of increasing and decreasing porosity linked to the overlap of more or less dense aggregates in bentonite with a size of less than 5 mm.

The evolution of the porosity in the concrete displays an increase in the direction of the interface over a thickness of 15 mm (Fig. 3). The 500 pixel-wide profile shows an increase in the total mean porosity up to 70%, while after this thickness of 15 mm, the porosity in the concrete decreases down to 40%. The porosity profile computed with the 10 pixel width brings out a more precise evolution of the porosity with a higher overall range. At the interface, the porosity ranges from 100% down to 10%, indicating the presence of macropores and the cross-cutting of small aggregates, respectively. Over this thickness of 15 mm, numerous pixels have a porosity ranging from 60 to 80%. This porosity domain reflects the porosity of the cement binder in between the non-porous grains. The porosity of the cement binder in the concrete, centimeters from the interface, ranges between 30 and 40%, in agreement with the porosity histograms (Fig. 2). The porosity values below and above this range are linked to the cross-cutting of non-porous aggregates and voids. The porosity values at 0%, between 25 and 30 mm from the interface, indicates the presence of non-porous grains exceeding 100 μm, as illustrated in Fig. 1.

3.2. Chemical and mineralogical characterization

Based on the porosity evolution, from autoradiography data, chemical and mineralogical characterization focused on the concrete. As concrete is a heterogeneous material, with the presence of siliceous and/or carbonate aggregates, SEM images and chemical mapping can be used to distinguish and evaluate chemical variability in a zone near the bentonite interface. Chemical heterogeneities can be visualized and quantified through chemical mapping, while analysis from bulk or scraping sub-sampling could be non-representative considering the heterogeneity of the materials. The relative abundance of minor nanocrystalline phases should be smoothed by the integration of aggregates in the sub-sampling.

3.2.1. Qualitative element distributions

Large field of view EDX maps were acquired over the concrete in contact with the bentonite. Fig. 4 displays the backscattered electron (BSE) image of the mapped area and some associated EDX maps. EDX maps can be used to visualize the element distributions in the concrete at the centimeter scale. The BSE image reveals layering parallel to the interface, as shown in the autoradiography. Calcium and sulfur are depleted in the concrete matrix over a distance of ~3 mm from the interface, linked to the highest porosity zone in the concrete (Fig. 1) near the bentonite contact. Nonetheless, a sharp increase of calcium is observed in concrete over a thickness of hundred's μm in direct contact with bentonite. Also, magnesium and silicon appear to be enriched over 1–3 mm in concrete in contact with bentonite. In the bentonite, a small layer at the interface is enriched in calcium and magnesium. Element quantification with energy dispersive spectroscopy is strongly influenced by the inhomogeneous distribution of porosity. The spatial distribution of the chemical elements should thus be considered as a function of the porosity evolution, even if the depletion of calcium and sulfur does not seem to be correlated with the porosity distribution. Figs. 1 and 4 also show a layering of aggregates and voids, which is caused by the application of the shotcrete.

3.2.2. Mineralogical mapping from quantitative chemical maps

Taking into account the previous porosity results and chemical

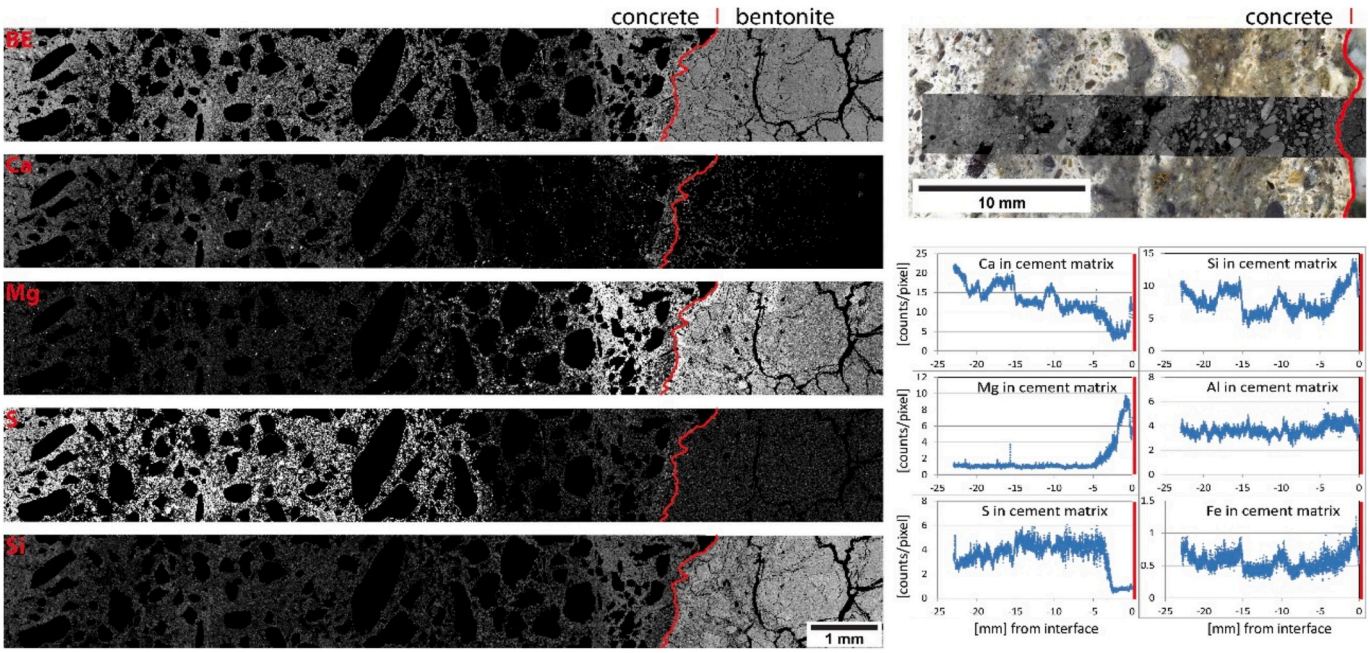

Fig. 4. Left: backscattered electron (BSE) microscopy image and Energy-Dispersive X-ray spectroscopy (EDX) element maps of concrete in contact with bentonite (aggregates, voids and cracks segmented in black). Right: overview reflective light microscopy image with BSE image inset and EDX elemental count profiles. Interface traced in red. (For interpretation of the references to color in this figure legend, the reader is referred to the Web version of this article.)

element distributions, two quantitative chemical maps were acquired from the autoradiography of the polished sections of concrete (Fig. 5). The first map was made 1 mm from the interface where the magnesium enrichment was observed, and the second 3 cm away from the interface, avoiding any heterogeneous chemical distribution due to textural induced changes during the initial shotcreting work. Fig. 5 displays the localization, the BSE images and some quantitative chemical maps, of the mapped areas. The chemical x-ray maps of Ca, Mg, S and Cl are given for each probed area. The same calibration bar was set for each element, allowing the direct comparison of false color intensity between the two mapped areas. Based on the comparison of the displayed quantitative chemical maps between both areas (Fig. 5), lower concentrations of calcium, sulfate and chloride can be identified at the interface, while the amount of magnesium increases. At the interface, Ca and Mg X-ray maps reveal anti-correlated layering parallel to the interface, so that when the atomic percentage of Mg increases that of Ca reduces and vice versa.

In the chemical ternary plots, built from the pixels of the 10 probed chemical maps, several clusters of pixels were identified. These clusters represented pixels with a similar chemical composition. Their stoichiometry was compared directly to the different mineral end-members for which their theoretical compositions were added to the projection (Fig. 6). The clusters are connected with lines or areas of pixels, which represent pixels mixing two or more minerals at the sub-μm scale (grain sizes smaller than the measurement volume).

The position of the clusters in the ternary projections differs between the two maps (Fig. 6). In the map made in the shotcrete distant from the interface, a large cluster is centered close to the theoretical composition of C–S–H with Ca/Si of 1.47 (Roosz et al., 2018), identified as C-A-S-H in Fig. 6. This cluster does not appear at all in the map acquired in the shotcrete at the interface. Instead, two large clusters, depleted in calcium, are identified. Likewise, clusters centered on AFm and AFt theoretical compositions are present in shotcrete while not at the interface. However, on both ternary plots, the same clusters spread along the Si and Al–Fe–Mg axis are observable.

The mineralogical maps were created based on the methodology developed by (Gaboreau et al., 2017). This methodology consists in identifying all the phases constituting the mapped area through a step-by-step process, combining a succession of projections into ternary diagrams and constraint on element content, from which contrasting chemical compositions for all the mineral and solid phases can be discriminated.

The first step of mineralogical mapping was to segment the pore network and the aggregates, considering the sum of atomic wt% in pixels (Gaboreau et al., 2017). As mentioned above, on both mapped areas, we identified the same clusters of pixels, corresponding to the aggregates. All the pixels of the aggregates were segmented using the polygon tool and were back-projected onto the BSE images. Among the selected clusters (Fig. 7), different minerals were identified, such as microcline, albite, micas, chlorite and quartz.

After the segmentation of the aggregates, the remaining pixels were plotted in the Si–Ca–AlFeMg ternary projection (Fig. 8). Theoretical chemical compositions of cement and hydrated phases were superimposed on the scatterplots to compare them to the chemical composition field of the different analyzed clusters. These representations allow the chemistry of the two mapped areas to be compared. In the shotcrete, centimeters from the interface, the chemical composition field of the clusters is close to some theoretical compositions of hydrates and cement phases. In this chemical projection (Fig. 8), clusters have compositions in agreement with AFt, AFm and hydrogarnet (Katoite). Some pixels are also spread up to the theoretical composition of hydrotalcite. The cluster positioned on the Ca pole could correspond to different minerals and phases (portlandite, calcite or gypsum). This displayed chemical projection (Fig. 8) does not allow them to be discriminated at this stage. Two large and joined clusters, close to the theoretical composition of C2S and C–S–H 1.47, constitute the main distribution of pixels of the shotcrete.

At the interface, none of the identified clusters corresponding to the hydrates in the shotcrete are observable. In return, two large clusters depleted in calcium are present. The only correspondence between both projections is the cluster centered on the Ca pole and the pixels spread to the ferrite (C4AF) end-member.

To build the quantitative mineral maps, a sequence of ternary projections were used as proposed in (Gaboreau et al., 2017). Fig. 9 displays the last steps of segmentation used to threshold the hydrates in the shotcrete. Different steps, using constraints in some chemical element concentrations (Fig. 9) were applied to threshold the hydrates and some

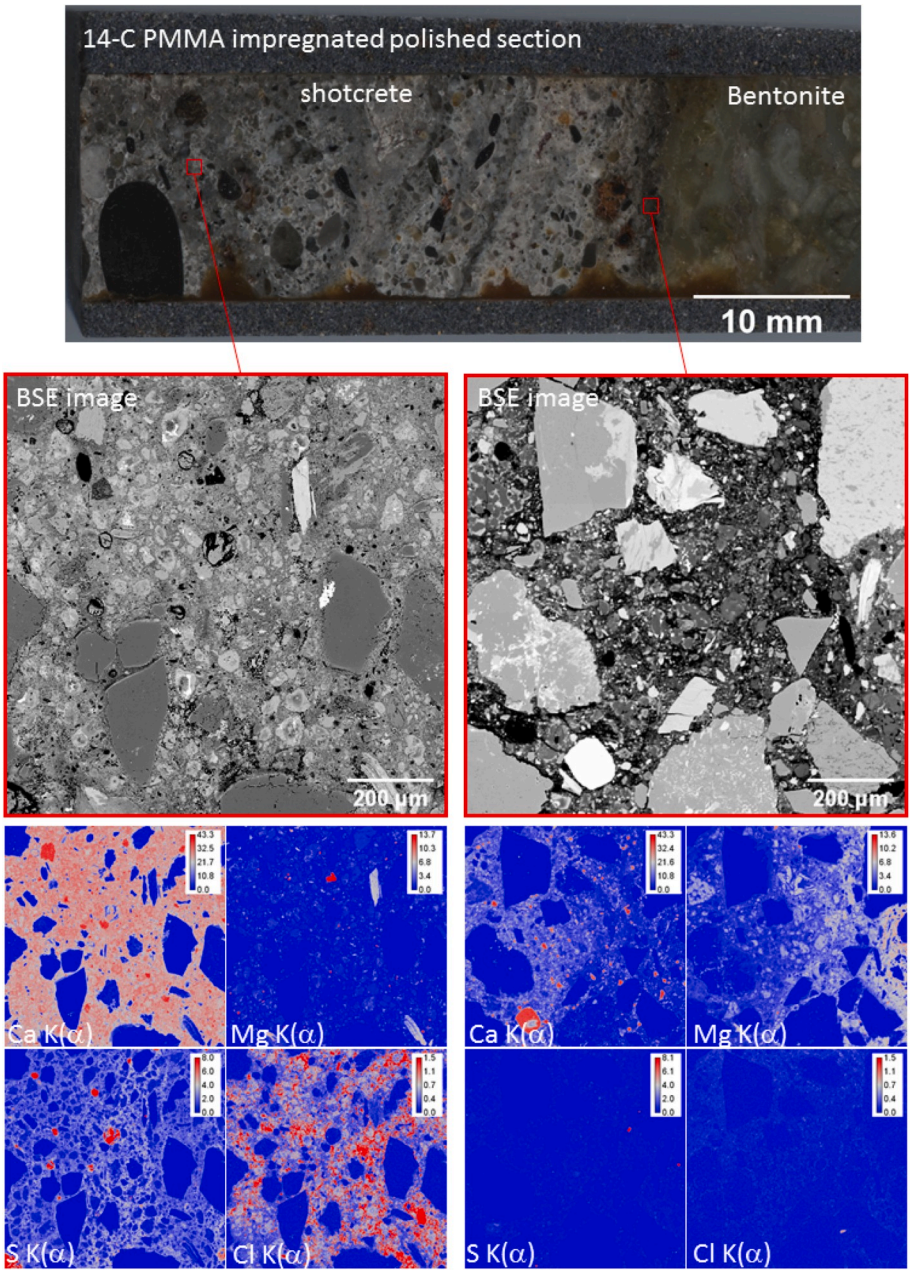

Fig. 5. Upper image: 14-C PMMA polished section and localization of the two mapped areas (red squares). Middle images: BSE images of the selected areas. Lower images: selected quantitative chemical maps of the two mapped areas. The calibration bars are given in atomic weight %. (For interpretation of the references to color in this figure legend, the reader is referred to the Web version of this article.)

residual non-hydrated cement grains. On the mineral map, each color corresponds to a phase thresholded from a cluster of pixels with distinct chemical composition. Residual clinker grains, like C4AF and also some grains with an intermediate chemical composition between pure belite and precursor hydrated C-A-S-H (Clinker low hydr. in the legend, Fig. 9), were identified. These latter grains have a sum of oxides lower than 80 wt% and are depleted in calcium (45 wt%, Table 1) with regard to the theoretical value of calcium oxides in belite (63 wt%, Taylor, 1992). These residual clinker grains were associated with rounded gray grains (Fig. 9), with chemical compositions close to C–S–H compositions (Roosz et al., 2016). The calculated chemical composition of these phases is $Ca_{1.52}Al_{0.1}Si_{0.9}O_{3.7}$ xH_2O. These C-A-S-H grains also appear with a higher brightness on the BSE image (Fig. 5), meaning a higher mean atomic number. Other phases, such as hydrogarnet, hydrotalcite, AFm and Aft, were also identified. All the chemical compositions and the weight fractions of each phase are given in Table 1. The hydrogarnet is mainly associated with the residual ferrite grains and has an intermediate composition between stratlingite and katoite. The chemical composition of AFm displays an anionic chloride occupation (Table 1). The anionic vacancy of the calculated formula ($Ca_4Al_2[Cl_{0.5}\square_{0.25}]O_8$ xH_2O) could be due to the presence of a carbonate group (CO_3^{2-}), as carbon is not analyzed with EPMA. The remaining cluster of pixels (step 4, Fig. 9) with a chemical composition close to the theoretical composition of C–S–H 1.47 (Roosz et al., 2018) corresponds to the cement binder (C-A-S-H/sulfate in the legend). The cluster was plotted into ternary diagrams with different chemical axes to discriminate the pixels with different chemical compositions. These pixels were plotted in the Si–Ca/3-AlS_3 diagram, to inspect the variation of the chemical composition of the matrix (Fig. 9). In this projection, the cluster was distributed along a line from the theoretical composition of C–S–H1.47 to the AFt or

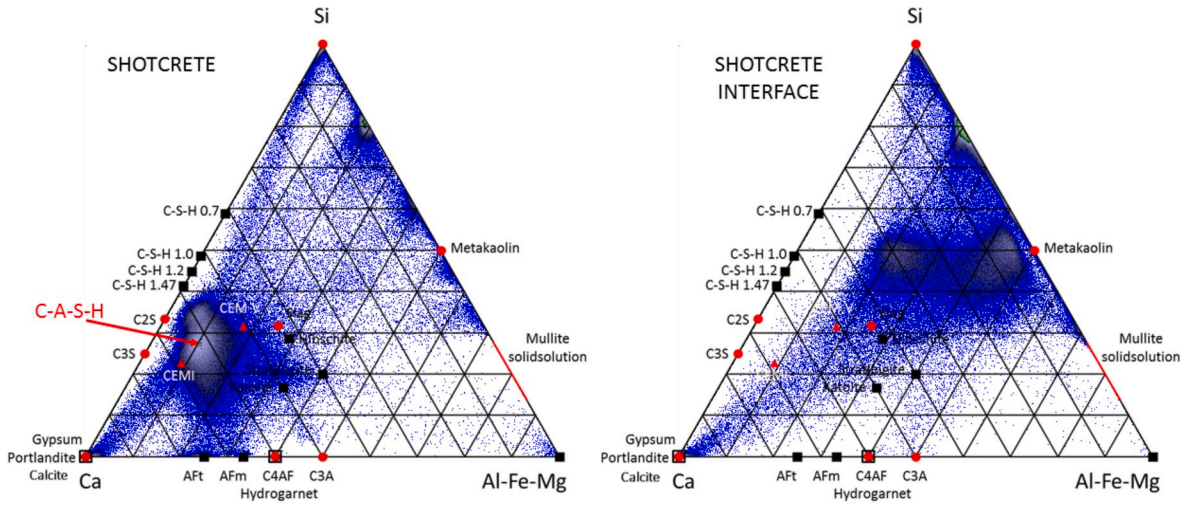

Fig. 6. Si–Ca–AlFeMg ternary projections of all the pixels of the mapped areas collected in the shotcrete and in the shotcrete at the interface. The main cement and hydrate phases end-members were added to the scatter plots (red and black symbols). (For interpretation of the references to color in this figure legend, the reader is referred to the Web version of this article.)

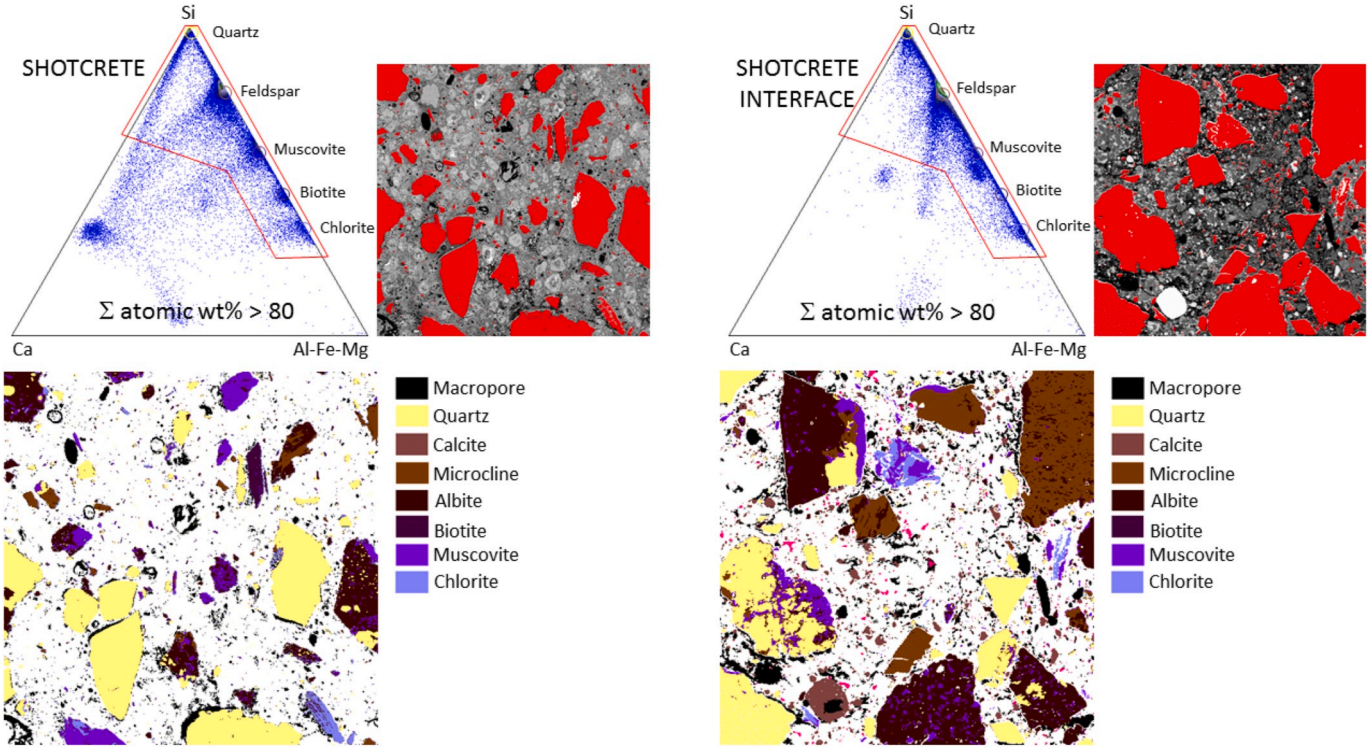

Fig. 7. Segmentation of the aggregates by polygon selection in ternary plots and back-projection onto the BSE images.

AFm phases, suggesting that the chemical compositions of the pixels could be a mixture of sulfate phases and C-A-S-H. The cluster was segmented into three domains, as illustrated in the ternary diagram of Fig. 9. The pixels with the lower sulfate concentration (in light gray, Fig. 9) were organized around the rounded gray grains of C-A-S-H while the two other domains were distributed on areas where the sulfate concentrations are high (sulfate map, Fig. 5).

On the quantitative mineral map built in the shotcrete at the interface, the same assemblage of aggregates was identified as in the previous map, centimeters from the interface. The quantity of each phase and their chemical composition are given in Table 2. After the segmentation of the aggregates (Fig. 7), two large clusters depleted in calcium remained and were plotted in the Si–Ca–AlFeMg and the M^{+}-4Si-R2 diagrams (Fig. 10). The latter is a ternary diagram used to discriminate the chemistry of di- and tri-octahedral phyllosilicates (Velde, 1985), where $M^{+} = Na + K + 2Ca$, $4Si = Si/4$ and $R^{2+} = Fe + Mg$. Some phyllosilicate end-members were superimposed onto both ternary representations (Fig. 10). In the Si–Ca–AlFeMg diagram, one of the two clusters is close to the theoretical compositions of phyllosilicates while the other seems to correspond to low Ca/Si C-A-S-H. By plotting these two clusters on the M^{+}-4Si-R2 diagram, one is close to the chemical composition of C–S–H and the second is stretched along a line between the M^{+} pole and the magnesium phyllosilicates. Like for the map done in the shotcrete, the weight fractions of some elements were used to discriminate the clusters of pixels with different chemical compositions. The first constraints were applied on calcium to extract the pixels with

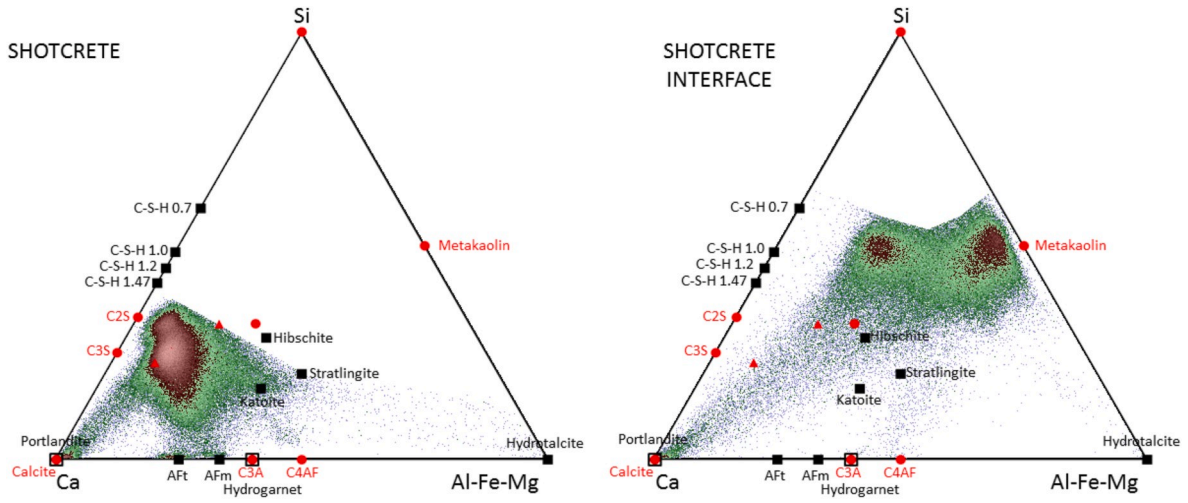

Fig. 8. Si–Ca–AlFeMg ternary plots with the remaining pixels after the segmentation of the aggregates. The red and black symbols represent chemical compositions of cement phases and hydrates, respectively. (For interpretation of the references to color in this figure legend, the reader is referred to the Web version of this article.)

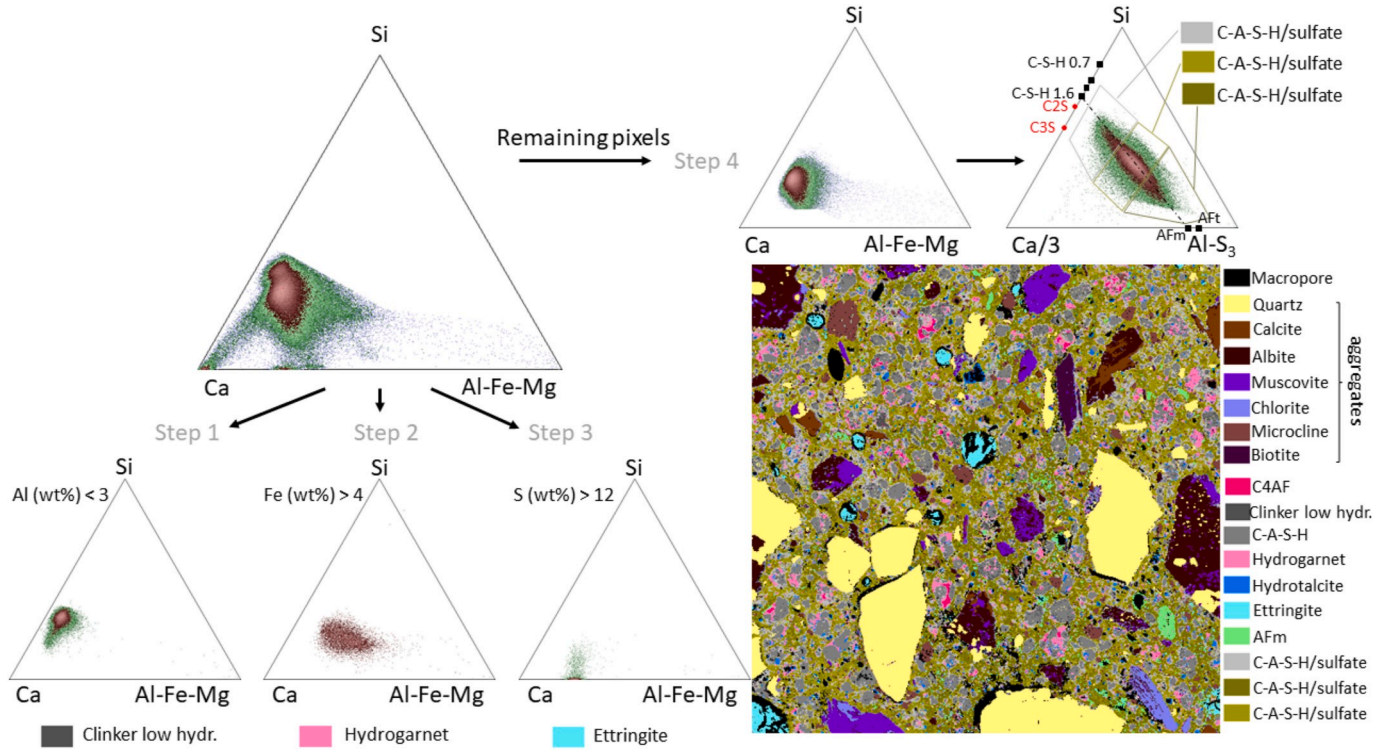

Fig. 9. Ternary plots displaying the thresholding methodology for the pixels remaining after the segmentation of the aggregates and mineral map of the shotcrete distant from interface.

the highest content (CaO > 14 wt%, Fig. 10). These pixels were organized on the left of the map, at the opposite end from the direct contact with the bentonite. Inversely, by selecting the pixels with the highest content in magnesium, the pixels were distributed on the side in contact with the bentonite (in blue, MgO > 11 wt%, Fig. 10). All the selected pixels were back-projected on the BSE map, verifying the accuracy of the selection with regard to the shape of the grains identified in the BSE image. The other phases are distributed between these two extremes. Nonetheless, one of these two clusters seems to be linked to the decalcification of shotcrete C-A-S-H, while the other represents a second reactive pathway. The chemical composition of each phase is given in Table 2. The high porosity of this area means that the sum of oxides of the analyzed pixels is low, due to the integration of voids in the probed volume (Gaboreau et al., 2017; Pret et al., 2010a). The weight fraction is not given for this map due to the non-identified phases and hence the lack of knowledge of the grain density.

To identify the possible mineral corresponding to the analyzed chemical compositions (Table 2), ternary diagrams with different chemical axes were used. In the M^{+}-4Si-R2 diagram, the cluster stretched toward compositions of Mg phyllosilicates was plotted on a 3Ca–SiFeMg–4Al ternary scatterplot. This diagram dissociates the tetrahedral charge from the octahedral charge in phyllosilicate. In this representation, the cluster is stretched along a line half dividing di- and tri-tetrahedral charged phyllosilicates whose ends are 3Ca and

Table 1
Minerals and solid phases identified in the mapped area of the shotcrete with the volume and weight fraction and the chemical composition of each component.

	Mineral/phases	Volume (%)	Weight (%)	Weight (%)	Analyzed chemical composition (wt%)								
					CaO	SiO_2	Al_2O_3	Fe_2O_3	MgO	SO_3	ClO	K_2O	Na_2O
Macroporosity		4.8											
Aggregates	Quartz	13.8	15.5			100							
	Microcline	1.1	1.2			66	17					17	
	Albite	6.4	7.1		1	70	18						11
	Biotite	1.5	1.8										
	Muscovite	3	3.6			52	24	4	2			11	
	Chlorite	0.6	0.7			31	18	26	12				
	Calcite	3	3.6		52								
Hydraulic binder phases (Fig. 9)	Clinker low hydrated	1.9	2.6	3.9	45	28	1.5	1					
	C4AF	0.5	0.7	1.1	44	14	20	21					
	Hydrogarnet	4	4.7	7.1	32	14	18	4					
	Hydrotalcite	1.6	1.4	2.1			15		38				
	AFm	1.2	0.9	1.4	38		14	21			4		
	AFt	1.5	1.1	1.7	38		10			22			
	C-A-S-H	11.2	13.3	20.0	42	26	2	4					
	C-A-S-H mixed with sulfate (1)	11.4	11.6	17.4	40	20	4	2		4			
	C-A-S-H mixed with sulfate (2)	12	11.2	16.8	38	17	4	1.5		5.5			
	C-A-S-H mixed with sulfate (3)	20.5	19.1	28.7	36	13	6	1.5		7			
	Sum	100	100										
	Sum hydraulic binder	65.8	66.6	100									

Table 2
Minerals and phases identified in the mapped area of the shotcrete at the interface (Fig. 10) with the volume fraction and the chemical composition of each phase. The phases referenced xx > At wt% are for phases for which no mineral names could be assigned at this stage. The identification is done with the contrast At wt% of each phase.

	Mineral/phases	Volume (%)	Volume (%)	Analyzed chemical composition (wt%)								
				CaO	SiO_2	Al_2O_3	Fe_2O_3	MgO	SO_3	ClO	K_2O	Na_2O
Macroporosity		7										
Aggregates	Quartz	12			100							
	Microcline	10.7			66	17					17	
	Albite	18.6		1	70	18						11
	Biotite											
	Muscovite	3.9			52	24	4	2			11	
	Chlorite	1.7			31	18	26	12				
	Calcite	6.8		52								
Hydraulic binder phases (Fig. 10)	C4AF	0.6	1.5	44	14	20	21					
	Fe oxy/hydroxides	0.05	0.1				70					
	Al > 15 wt%	1.1	2.8	3	44	15	4	11				
	Ca > 14 wt%	8.8	22.4	14	28	7	1.5	2				
	Ca > 11 wt%	6.2	15.8	11	22	7	2	3				
	Mg > 11 wt%	1.9	4.8	3	32	9	4	11				
	Mg > 8 wt%	8.3	21.1	4	31	9	3	8				
	Fe > 8 wt%	1	2.5	9	22	11	8	5				
	Mixed composition	11.3	28.8	3–14	20–32	4–12	2–3	2–12				
	Sum	100										
	Sum hydraulic binder	39.25	100									

vermiculite. The calculated formulas for these Mg-rich phases are:

Mg sup 11 $Ca_{0.32}(Si_{3.25}Al_{0.75})^{IV}[Al_{0.35}Mg_{1.85}Fe_{0.25}]^{VI}\ O_{10}(OH)_2$

Al sup 15 $Ca_{0.26}(Si_{3.45}Al_{0.55})^{IV}\ [Al_{0.85}Mg_{1.25}Fe_{0.22}]^{VI}\ O_{10}(OH)_2$

They are compatible with 2:1 phyllosilicates combining tri- and di-octahedral character as it is depicted in the 3Ca–SiFeMg/4-Al plot.

4. Discussion

The precise description of the modification of mineral assemblages to be developed at the pore scale in the EBS reactive interfaces is a key issue to build reliable predictive modelling exercises, carried out to gain confidence in the long term safe performance of these systems. The most studied geochemical systems concerning EBS repository stability are (i) the evolution of phases involved in the long-term hydration reaction of the cement/water paste (Fernández et al., 2018a; Ridi et al., 2011), (ii) the role of the formation of disordered hydrated Mg-silicate phases (M-S-H) in concrete interaction with near-neutral pH pore waters in granite or clay rocks (García Calvo et al., 2010; Lothenbach et al., 2015), (iii) neogenic phase formation (i.e, C-A-S-H; zeolites, authigenic Mg-(Al)-silicates) at the interface between clay materials and concrete in zone with contrasted pore water chemistry (Cuevas et al., 2006; Fernández et al., 2016; Jackson et al., 2017). Related phenomena such as the possibility of clay pore-clogging promoting a low hydration rate

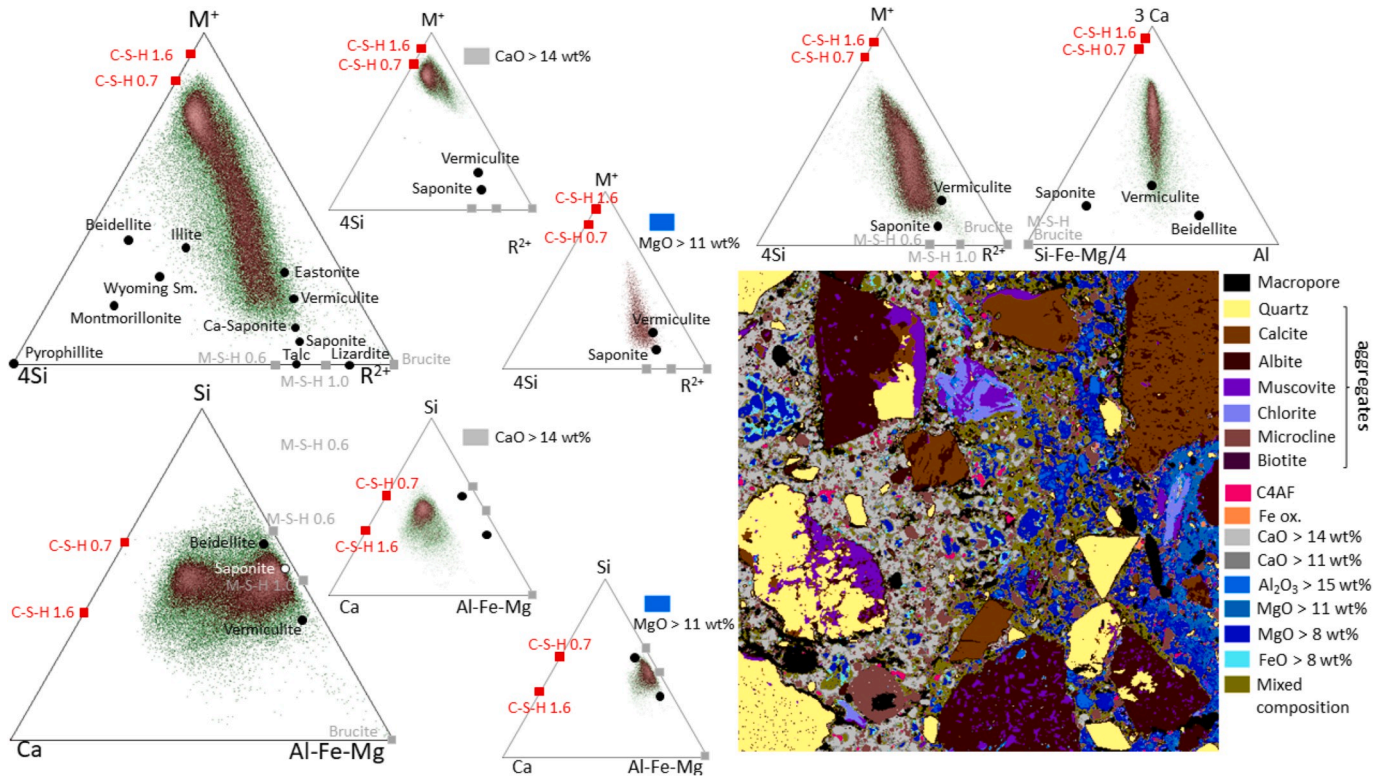

Fig. 10. Ternary plots thresholding methodology for the pixels remaining after the segmentation of the aggregates and mineral map of the shotcrete at the interface.

and swelling of the bentonite barrier, the durability of concrete affected by bentonite or clay saline pore waters, or the chemical buffering role of the precipitation are important geochemical consequences to the integrity of the multi barrier concept.

In such a way, mineralogical mapping has proven to be a powerful tool to depict and spatialize the chemical perturbation at interface between contrasted materials. It allows the chemical evolution of a system to be spatialized and quantified and identifies the precise chemical composition phases whatever their amount and crystallinity. Bearing in mind that 1 × 1 mm^2 mapping zones rule out large grains of calcite, quartz, feldspars, schist rock, etc., the micro-aggregate composition in both examined zones captures the predominance of quartz, albite and calcite, where K-feldspar, muscovite and biotite are present, which is very consistent with the semi-quantitative X-Ray Diffraction (XRD) determination (Turrero and Cloet, 2017). The abundance of AFt grains (ettringite) and Cl-rich AFm (Florea and Brouwers, 2012) in the concrete binder, outside the 2 cm interface rim, characterizes the less porous centimeters compared to the interface zone. Chloride adsorption in AFm-like phases has been previously deduced in laboratory studies of cementitious materials hydrated with a saline chloride rich water in contact with FEBEX bentonite (Cuevas et al., 2016). Therefore, the distribution of mineral grains in this zone is consistent with the complex cementitious material formulation due to the increased amount of accelerant Al-sulfate additives, producing the precipitation of secondary ettringite (blue balls in Fig. 9) and a lot of small sulfates mixed with the C-A-S-H phases.

No discrete portlandite is found in the concrete centimeters from the interface, in agreement with its dissolution (Alonso et al., 2017) and subsequent formation of secondary ettringite and presumably calcite (Glasser and Matschei, 2007), in the presence of granitic or bentonite (bicarbonate-rich) hydrating pore waters. However, signs of heterogeneous hydration reactions are evidenced by the existence of poorly hydrated grains (presence of grains keeping the shape of old clinker grains in binder areas of Fig. 9). The rapid formation of C-A-S-H favored by the presence of the Al-sulfate source produced a C-A-S-H coating that could induce a slow hydration rate of clinker anhydrous grains. According to (Garrault et al., 2011; Pustovgar et al., 2017), the precipitation of C-A-S-H silicate hydrates instead of C–S–H can retard and passivate hydration because they are not a good substrate for further C–S–H growth. Again, chemical-mineralogical mapping gives specific reactivity details related to the application of the shotcrete material.

The reactivity of the concrete at the bentonite interface is affected by the porosity distribution (Fig. 1). Qualitative EDX scans show sharp zonation drawn for Ca, S, Mg and Si distributions. The first 1–3 mm of concrete adjacent to bentonite are depleted in Ca and S, with a sharp enrichment in Mg, Si and relatively in Al and Fe, while Ca is concentrated in the bentonite "wall" due to the frequently observed precipitation of calcite (Fernández et al., 2017). The bentonite zone is characterized by a porosity area that is rather homogeneous (40–60% porosity). Taking into account that the specific weight of bentonite is 2.7 g/cm^3 and the dry density of bentonite measured at the interface is 1.5 g/cm^3 (Turrero and Cloet, 2017), this corresponds to a porosity of 45%, in agreement with the autoradiography results (Figs. 1 and 2). In the concrete, the Si–Mg enrichment (depleted in Ca and S) zone is located within the ~3 mm where the porosity is 60–80%, near the bentonite interface (Figs. 2 and 3). This layer could be explained by the shotcrete application (layers with large air voids, or with low degree of hydration, but also Ca and S-depleted layers) or by interaction with the bentonite (decalcification and S depletion right at the interface). On the one hand, Ca and S depletion have been shown to be characteristic of OPC interaction with Opalinus Clay (Dauzeres et al., 2016; Jenni et al., 2014; Mäder et al., 2017); however Mg enrichment is characteristic solely in clayrock or bentonite for OPC, and in both when low pH cement is used (Jenni et al., 2014). In this case, the Mg–Si zone, according to the mineralogical map (Fig. 10), is related to porosity filling with mineral phases composed of elements coming from the bentonite (Mg, Al, Si). It suggests that at the application of the shotcrete (highly fluid shotcrete application, induced by a high w/c ratio), a relatively high porosity zone acted as a preferential fluid flow path in which leaching and precipitation processes of dissolved species from bentonite have taken place. The

existence of a preferential reactive pathway in this zone is evidenced by the mixing of granite, bentonite and concrete pore waters characterizing sharp anomalies of $\delta^{18}O$ and $\delta^{13}C$ stable isotope signatures of carbonates at the scale of the whole FEBEX experiment interface measured on more than 8 samples (Torres et al., 2019).

Although the porosity increase at the interface can bias the quantification of mineral distribution, from a qualitative point of view the binder of this zone contains intimate nanoscale mixtures of Ca-phases (calcite), Ca silicate hydrates, and Mg–Al silicate phases (Table 2), with a significant increase in calcite precipitation and the apparent absence of biotite, presumably altered in this special reactive zone. Characterization tests by means of XRD and Fourier-Transform Infrared Spectroscopy (FTIR), applied to sample scrapings and ultrasonic dispersion practiced to be able to extract pore minerals, in these zones (not shown in this paper), reveal complex mixtures of montmorillonite, calcite and apparently tri-octahedral neogenic clay minerals consistent with the Si–Mg anomalies. These data poorly resolved the nature of the phases formed. In the case of the alteration in the bentonite phase, bulk chemical data extracted from EDX area profiles have shown the possibility of the formation of stevensite-saponite-like minerals coexisting with brucite-montmorillonte mixtures (Cuevas et al., 2018). Unfortunately the pervasive mixing with montmorillonite only allowed compositional trends to be identified and not precise compositions.

The precipitation of Mg-phases and Mg silicates at the clay-concrete interface have been expected in many predictive studies, including reactive transport modelling (Marty et al., 2014). Brucite is commonly predicted to precipitate in the concrete pores in contact with the clay interface (Samper et al., 2018). However, the clay-concrete interfaces used to predict the precipitation of hydrotalcite, sepiolite or saponite depend on the minerals considered to be involved in the thermodynamic system (Marty et al., 2009, 2015; Samper et al., 2018). In natural conditions, Mg/Si clays, such as palygorskite and sepiolite, form in low saline environments, near neutral pH conditions. Smectites (intermediate Mg/Si kerolite-stevensite to saponite) may form in moderate saline high pH (>9) local environments. Stevensite (smectite with octahedral vacancies) or saponite (if soluble Al is available) is favored at higher pH (>9.5) (Eberl et al., 1982; Jones and Galán, 1988; Tosca and Masterson, 2018). The use of more common natural minerals such as saponite to check the very long term evolution of these environments seems to yield reliable results compatible with the evolution of natural clays to form chlorite and illite during diagenesis (Meunier, 2005). The use of saponite or Mg-silicate hydrate precursor is also consistent if stability or predominance diagrams are built to test the compatibility of Mg/Si phases with low Ca/Si (<0.8) C-(A)-S-H, such as those formed in the studied interface. Ca-saponite or Mg/Si 1.2–0.6 Mg-silicate hydrates overlapped in stability fields (Roosz et al., 2015, 2018).

In this case, we depicted the formation of Mg-clay minerals in the high porous concrete area. Discrete areas were characterized using a quantitative chemical-mineralogical mapping methodology and autoradiography results. This resulted in two separate chemical formulas described in the results section. Other evidence of Mg-clay phase precipitation (Lerouge et al., 2017), in concrete at the interface with Opalinus clay, was displayed with high charge 2:1 tri-di-octahedral sheet silicate including octahedral vacant sites, as the phase formed in this interface reaction system. In our case, the mixing character between di- and tri-octahedral 2:1 sheet silicates is consistent with a positive correlation between the tri-octahedral character and the increase in tetrahedral charge, which is a typical feature of saponite or vermiculite. Vermiculite, whose origin is related to biotite alteration, used to be tri-octahedral, and often exhibits an excess of positive octahedral charge (Valkov and Simha, 2012). Lerouge et al. (2017) have argued that mixed tri-di mineral with vacant sites such as in stevensite smectites, which implies there is a trend in which Mg content is not correlated with tetrahedral charge increase.

In order to discuss the nature of the Mg–Al-Clay formed, we made calculations using mixtures of trioctahedral Mg-vermiculite (0.8 charge per $O_{10}(OH)_2$ structure), montmorillonite (i.e. FEBEX composition), beidellite (0.5 layer charge) and saponite (0.5 layer charge). We also used intermediate compositions isolated in the Mg–Al clay region during the segmentation process (Mg sup 10 and Mg sup 8 in Fig. 10 legend). The calculated compositions lie in a linear mix trend between tri-octahedral vermiculite and beidellite (Fig. 11). In fact, tri-octahedral Mg vermiculite can be considered as a saponite, in as far as saponites with layer charge in the magnitude of vermiculite have swelling properties equivalent to smectite minerals (Michot et al., 2005; Suquet et al., 1977). The composition obtained is thus formally consistent with a vermiculite/beidellite mixture.

5. Conclusion

The reactivity of concrete-clay interfaces has been long studied to assess the degradation of such geochemical contrasted engineered and natural barriers. Laboratory experiments, natural analogues, in situ interfaces and geochemical reactive transport modeling have been implemented to robustly predict their behavior over decades. Many of these studies were conducted on homogeneous model reactive systems, while heterogeneities, nature and sources are expected to exist at the interface between the engineered barriers, and linked to the elasto-plastic nature of the materials and man-made intervention.

The FEBEX project is an in situ experiment mimicking the storage of canisters (heater sources) with the different engineered barriers used to confine them and the different man-made intervention to construct a scale 1 experiment.

To characterize such complex and heterogeneous interfaces, a spatial downscaling approach was used to evaluate the reactivity of the shotcrete barriers. The methodology is based on 2D quantitative porosity mapping that spatialized microstructure evolution for pluri-centimetric samples with micrometric resolution. Coupled with large field chemical element distribution, screening of the sample allows us to focalize on region of interest to more accurately depict the geochemical reactivity with quantitative mineral mapping. The mineral distribution of concrete near a bentonite interface based on the FEBEX experiment has been

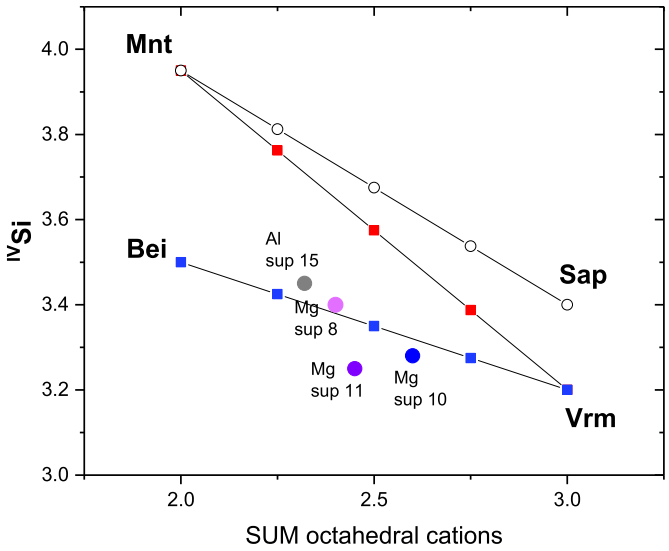

Fig. 11. Mixing trends drawn by linear combinations of 0.25, 0.5 and 0.75 fraction components of montmorillonite (open circles and red squares) or beidellite (blue squares) with complementary ratios of saponite (0.5 (+) charge O10(OH)2, all Al tetrahedral)) or trioctahedral vermiculite ((0.8 (+) charge O10(OH)2, all Al tetrahedral)). Al sup 15 (Al > 15%), Mg sup 8 (Mg>8%), and Mg sup 11 (Mg>11%) data are in Table 2. Abbreviations Mnt, Sap, Bei and Vrm are for Montmorillonite, Saponite, Beidellite and Vermiculite, respectively. (For interpretation of the references to color in this figure legend, the reader is referred to the Web version of this article.)

described in detail, applying the combination of autoradiography, large field EDX mapping and discrete quantitative EPMA/mineral maps. This approach allows us to obtain spatialized information, geolocalize the region of interest from porosity data and avoid any random sub-sampling. Quantitative porosity mapping allowed us to relate, at least partially, the consequences of how the shotcrete was applied, with the porosity zonation at the interface creating a preferential flow path.

Such high porous areas could affect the reactive process, accelerating leaching and diffusion and related dissolution/precipitation reactions. As described recently in an equivalent concrete/clay interface, magnesium enrichment and calcium leaching are the main chemical reactions that occur in concrete at the interface. In Mg-rich areas, M-S-H were described as potential precipitating phases (Dauzeres et al., 2014), considering that they were related to cement phases, with the annotation system like C–S–H, with an Ca–Mg exchange (Bernard et al., 2018a, 2018b). More recently, they were characterized to be low crystalline 2:1 Mg phyllosilicate (Roosz et al., 2015). In the present study, quantitative chemical mapping and the associated chemical composition of identified phases allow us to depict the reaction pathway with the decalcification of cement phases and the precipitation of neoformation of di/tri mixed layer of beidellite and vermiculite.

These interfaces indicate that, in an in situ set up, heterogeneities could occur and lead to variable reactive pathways. Nonetheless, with regard to all the studies conducted on cement/clay interaction, and even if heterogeneities may exist, they do not impact the geochemical behavior over a long distance, as previously described. However, no information could be obtained at this stage on the mechanical behavior of materials considering the heterogeneities and the variable porosity distribution.

Likewise, tri-octahedral vermiculite/beidellite mixed layers were identified as phases precipitating in altered concrete at the interface, confirming (i) the previous observation made at other in situ cement/clay interfaces (Lerouge et al., 2016) and (ii) the different reactive transfer models used to predict the geochemical evolution of the interface. Considering the complexity of the phase assemblage, in terms of size and crystallinity, of the phases precipitating at 25 °C, intermixed with other potential nanosized phases, additional characterization at nanometer scale could validate the work initiated here.

Declaration of competing interest

None.

Acknowledgments

The research leading to these results has received funding from the European Union's Horizon 2020 Research and Training Programme of the European Atomic Energy Community (EURATOM) (H2020-NFRP-2014/2015) under grant agreement n° 662147 (CEBAMA). The FEBEX-DP Consortium (Nagra, SKB, Posiva, Ciemat, Kaeri) financed the dismantling and sampling operation in 2015.

References

Alonso, M.C., García Calvo, J.L., Cuevas, J., Turrero, M.J., Fernández, R., Torres, E., Ruiz, A.I., 2017. Interaction processes at the concrete-bentonite interface after 13 years of FEBEX-Plug operation. Part I: concrete alteration. Phys. Chem. Earth, Parts A/B/C 99, 38–48.

Bernard, E., Dauzères, A., Lothenbach, B., 2018a. Magnesium and calcium silicate hydrates, Part II: Mg-exchange at the interface "low-pH" cement and magnesium environment studied in a C-S-H and M-S-H model system. Appl. Geochem. 89, 210–218.

Bernard, E., Lothenbach, B., Cau-Dit-Coumes, C., Chlique, C., Dauzères, A., Pochard, I., 2018b. Magnesium and calcium silicate hydrates, Part I: investigation of the possible magnesium incorporation in calcium silicate hydrate (C-S-H) and of the calcium in magnesium silicate hydrate (M-S-H). Appl. Geochem. 89, 229–242.

Bildstein, O., Claret, F., 2015. Chapter 5 - stability of clay barriers under chemical perturbations. In: Tournassat, C., Steefel, C.I., Bourg, I.C., Bergaya, F. (Eds.), Developments in Clay Science. Elsevier, pp. 155–188.

Bullard, J.W., Jennings, H.M., Livingston, R.A., Nonat, A., Scherer, G.W., Schweitzer, J. S., Scrivener, K.L., Thomas, J.J., 2011. Mechanisms of cement hydration. Cement Concr. Res. 41, 1208–1223.

Caballero, E., Jiménez de Cisneros, C., Huertas, F.J., Huertas, F., Pozzuoli, A., Linares, J., 2005. Bentonites from Cabo de Gata, Almería, Spain: a mineralogical and geochemical overview. Clay Miner. 40, 463–480.

Chagneau, A.l., Tournassat, C., Steefel, C.I., Bourg, I.C., Gaboreau, S.p., Esteve, I.n., Kupcik, T., Claret, F., Schäfer, T., 2015. Complete restriction of 36Cl–diffusion by celestite precipitation in densely compacted illite. Environ. Sci. Technol. Lett. 2, 139–143.

Chapman, N.A., 2019. Who might Be interested in a deep borehole disposal facility for their radioactive waste? Energies 12, 1542.

Cloet, V., Turrero, M.J., 2019. Concrete ageing, concrete/bentonite and concrete/rock interaction analysis. In: 16-18, N.R.A.N., p. 282pp. Nagra Report Arbeitsericht NAB 16-18.

Cuevas, J., Ruiz, A., Fernández, R., González-Santamaría, D., Angulo, M., Ortega, A., Torres, E., Turrero, M., 2018. Authigenic clay minerals from interface reactions of concrete-clay engineered barriers: a new perspective on Mg-clays formation in alkaline environments. Minerals 8, 362.

Cuevas, J., Ruiz, A.I., Fernández, R., Torres, E., Escribano, A., Regadío, M., Turrero, M.J., 2016. Lime mortar-compacted bentonite–magnetite interfaces: an experimental study focused on the understanding of the EBS long-term performance for high-level nuclear waste isolation DGR concept. Appl. Clay Sci. 124–125, 79–93.

Cuevas, J., Vigil de la Villa Mencía, R., Ramírez, S., Sánchez, L., Fernández, R., Leguey, S., 2006. The alkaline reaction of FEBEX bentonite: a contribution to the study of the performance of bentonite/concrete engineered barrier system. J. Iber. Geol. 32, 147–169, 2006.

Dauzeres, A., Achiedo, G., Nied, D., Bernard, E., Alahrache, S., Lothenbach, B., 2016. Magnesium perturbation in low-pH concretes placed in clayey environment—solid characterizations and modeling. Cement Concr. Res. 79, 137–150.

Dauzeres, A., Le Bescop, P., Cau-Dit-Coumes, C., Brunet, F., Bourbon, X., Timonen, J., Voutilainen, M., Chomat, L., Sardini, P., 2014. On the physico-chemical evolution of low-pH and CEM I cement pastes interacting with Callovo-Oxfordian pore water under its in situ CO2 partial pressure. Cement Concr. Res. 58, 76–88.

Eberl, D.D., Jones, B.F., Khoury, H.N., 1982. Mixed-layer kerolite/stevensite from the amargosa desert, Nevada. Clay Clay Miner. 30, 321–326.

ENRESA, 1995. Almacenamiento geológico profundo de residuos radiactivos de alta actividad (AGP), Diseños conceptuales genéricos. Publicación Técnica ENRESA, Madrid, p. 105, 11/95.

ENRESA, 2006. FEBEX Project Final Report. Post-mortem Bentonite Analysis. Enresa publicación técnica, Madrid.

Fernández, Á., Lothenbach, B., Alonso, M.C., García Calvo, J.L., 2018a. Thermodynamic modelling of short and long term hydration of ternary binders. Influence of Portland cement composition and blast furnace slag content. Construct. Build. Mater. 166, 510–521.

Fernández, A.M., Baeyens, B., Bradbury, M., Rivas, P., 2004. Analysis of the porewater chemical composition of a Spanish compacted bentonite used in an engineered barrier. Phys. Chem. Earth, Parts A/B/C 29, 105–118.

Fernández, R., González-Santamaría, D., Angulo, M., Torres, E., Ruiz, A.I., Turrero, M.J., Cuevas, J., 2018b. Geochemical conditions for the formation of Mg silicates phases in bentonite and implications for radioactive waste disposal. Appl. Geochem. 93, 1–9.

Fernández, R., Ruiz, A.I., Cuevas, J., 2016. Formation of C-A-S-H phases from the interaction between concrete or cement and bentonite. Clay Miner. 51, 223–235.

Fernández, R., Torres, E., Ruiz, A.I., Cuevas, J., Alonso, M.C., García Calvo, J.L., Rodríguez, E., Turrero, M.J., 2017. Interaction processes at the concrete-bentonite interface after 13 years of FEBEX-Plug operation. Part II: bentonite contact. Phys. Chem. Earth, Parts A/B/C 99, 49–63.

Florea, M.V.A., Brouwers, H.J.H., 2012. Chloride binding related to hydration products. Cement Concr. Res. 42, 282–290.

Gaboreau, S., Lerouge, C., Dewonck, S., Linard, Y., Bourbon, X., Fialips, C.I., Mazurier, A., Pret, D., Borschneck, D., Montouillout, V., Gaucher, E.C., Claret, F., 2012. In-situ interaction of cement paste and shotcrete with claystones in a deep disposal context. Am. J. Sci. 312, 314–356.

Gaboreau, S., Prêt, D., Montouillout, V., Henocq, P., Robinet, J.-C., Tournassat, C., 2017. Quantitative mineralogical mapping of hydrated low pH concrete. Cement Concr. Compos. 83, 360–373.

Gaboreau, S., Pret, D., Tinseau, E., Claret, F., Pellegrini, D., Stammose, D., 2011. 15 years of in situ cement-argillite interaction from Tournemire URL: characterisation of the multi-scale spatial heterogeneities of pore space evolution. Appl. Geochem. 26, 2159–2171.

Gallé, C., 2001. Effect of drying on cement-based materials pore structure as identified by mercury intrusion porosimetry - a comparative study between oven-, vacuum-, and freeze-drying. Cement Concr. Res. 31, 1467–1477.

García Calvo, J.L., Hidalgo, A., Alonso, C., Fernández Luco, L., 2010. Development of low-pH cementitious materials for HLRW repositories: resistance against ground waters aggression. Cement Concr. Res. 40, 1290–1297.

Garrault, S., Nonat, A., Sallier, Y., Nicoleau, L., 2011. On the origin of the dormant period of cement hydration. In: 13th International Congress on the Chemistry of Cement, Madrid.

Glasser, F.P., Matschei, T., 2007. Interactions between portland cement and carbon dioxide. In: International Congress on the Chemistry of Cement-Cd-Rom Edition, Montréal, QC, Canada. TH3-13.14.

Goldstein, J.I., Newbury, D.E., Echlin, P., Joy, D.C., Romig, A.D.J., Lyman, C.E., Fiori, C., Lifshin, E., 1992. Scanning Electron Microscopy and X-Ray Microanalysis, second ed. Plenum Press, New York, NY.

Hellmuth, K.H., Siitari-Kauppi, M., Lindberg, A., 1993. Study of porosity and migration pathways in crystalline rock by impregnation with 14C-polymethylmethacrylate. J. Contam. Hydrol. 13, 403–418.
Huertas, Fariñas, Farias, García-Siñeriz, J.L., Villar, M., Fernández, A., Martin, P.-L., Elorza, Gens A., Sánchez, M., Lloret, A., Samper, J., Martínez, 2006. FEBEX-Full-scale Engineered Barriers Experiment. Updated Final Report 1994–2004.
Jackson, M.D., Mulcahy, S.R., Chen, H., Li, Y., Li, Q., Cappelletti, P., Wenk, H.-R., 2017. Phillipsite and Al-tobermorite mineral cements produced through low-temperature water-rock reactions in Roman marine concrete. Am. Mineral. 102, 1435–1450.
Jenni, A., Mäder, U., Lerouge, C., Gaboreau, S., Schwyn, B., 2014. In situ interaction between different concretes and Opalinus Clay. Physics and Chemistry of the Earth, Parts A/B/C 70– 71, 71–83.
Jones, B.F., Galán, E., 1988. Sepiolite and palygorskite. In: Bayley, S.W. (Ed.), Hydrous Phyllosilicates (Exclusive of Micas). Geochemical Society, pp. 631–674.
Lerouge, C., Gaboreau, S., Grangeon, S., Claret, F., Warmont, F., Jenni, A., Cloet, V., Mäder, U., 2017. In situ interactions between Opalinus clay and low alkali concrete. Phys. Chem. Earth, Parts A/B/C 99, 3–21.
Lerouge, C., Gaboreau, S., Grangeon, S., Roosz, S., Jenni, A., Mäder, U., Claret, F., Cloet, V., 2016. Opalinus Claystone-Low Alkali (LAC) Concrete Interaction: Mineralogical Investigations and Identification of a Mg-Rich Phase, Mechanisms and Modelling of Waste/Cement Interactions 2016 (Murten).
Lothenbach, B., Nied, D., L'Hôpital, E., Achiedo, G., Dauzères, A., 2015. Magnesium and calcium silicate hydrates. Cement Concr. Res. 77, 60–68.
Mäder, U., Detzner, K., Kober, F., Abplanalp, H., Baer, T., Cloet, V., 2016. FEBEX-DP – plug overcoring and concrete-bentonite interface sampling prior to dismantling. In: 16-10, N.r.N., p. 90. Nagra report. NAB 16-10.
Mäder, U., Jenni, A., Lerouge, C., Gaboreau, S., Miyoshi, S., Kimura, Y., Cloet, V., Fukaya, M., Claret, F., Otake, T., Shibata, M., Lothenbach, B., 2017. 5-year chemico-physical evolution of concrete–claystone interfaces, Mont Terri rock laboratory (Switzerland). Swiss J. Geosci. 110, 307–327.
Marty, N.C., Munier, I., Gaucher, E.C., Tournassat, C., Gaboreau, S., Vong, C.Q., Giffaut, E., Cochepin, B., Claret, F., 2014. Simulation of cement/clay interactions: feedback on the increasing complexity of modelling strategies. Transport Porous Media 104, 385–405.
Marty, N.C.M., Bildstein, O., Blanc, P., Claret, F., Cochepin, B., Gaucher, E.C., Jacques, D., Lartigue, J.-E., Liu, S., Mayer, K.U., Meeussen, J.C.L., Munier, I., Pointeau, I., Su, D., Steefel, C.I., 2015. Benchmarks for multicomponent reactive transport across a cement/clay interface. Comput. Geosci. 19, 635–653.
Marty, N.C.M., Tournassat, C., Burnol, A., Giffaut, E., Gaucher, E.C., 2009. Influence of reaction kinetics and mesh refinement on the numerical modelling of concrete/clay interactions. J. Hydrol. 364, 58–72.
Massat, L., Cuisinier, O., Bihannic, I., Claret, F., Pelletier, M., Masrouri, F., Gaboreau, S., 2016. Swelling pressure development and inter-aggregate porosity evolution upon hydration of a compacted swelling clay. Appl. Clay Sci. 124, 197–210.
Merlet, C., 1994. An accurate computer correction program for quantitative electron-probe microanalysis. Mikrochim. Acta 114, 363–376.
Meunier, A., 2005. In: Meunier, A. (Ed.), Clays in Sedimentary Environments. Clays. Springer-Verlag, pp. 295–325.
Michot, L.J., Bihannic, I., Pelletier, M., Rinnert, E., Robert, J.-L., 2005. Hydration and swelling of synthetic Na-saponites: influence of layer charge. Am. Mineral. 90, 166–172.
Nied, D., Enemark-Rasmussen, K., L'Hopital, E., Skibsted, J., Lothenbach, B., 2016. Properties of magnesium silicate hydrates (M-S-H). Cement Concr. Res. 79, 323–332.
Pokrovsky, O.S., Schott, J., 2004. Experimental study of brucite dissolution and precipitation in aqueous solutions: surface speciation and chemical affinity control. Geochem. Cosmochim. Acta 68, 31–45.
Pret, D., 2003. Nouvelles méthodes quantitatives de cartographie de la minéralogie et de la porosité dans les matériaux argileux : application aux bentonites compactées des barrières ouvragées. PhD thesis. Université de Poitiers, France, Poitiers, p. 257.
Pret, D., Sammartino, S., Beaufort, D., Fialin, M., Sardini, P., Cosenza, P., Meunier, A., 2010a. A new method for quantitative petrography based on image processing of chemical element maps: Part II. Semi-quantitative porosity maps superimposed on mineral maps. Am. Mineral. 95, 1389–1398.
Pret, D., Sammartino, S., Beaufort, D., Meunier, A., Fialin, M., Michot, L.J., 2010b. A new method for quantitative petrography based on image processing of chemical element maps: Part I. Mineral mapping applied to compacted bentonites. Am. Mineral. 95, 1379–1388.
Pustovgar, E., Mishra, R.K., Palacios, M., d'Espinose de Lacaillerie, J.-B., Matschei, T., Andreev, A.S., Heinz, H., Verel, R., Flatt, R.J., 2017. Influence of aluminates on the hydration kinetics of tricalcium silicate. Cement Concr. Res. 100, 245–262.
Ramirez, S., Cuevas, J., Vigil, R., Leguey, S., 2002. Hydrothermal alteration of "La Serrata" bentonite (Almeria, Spain) by alkaline solutions. Appl. Clay Sci. 21, 257–269.
Ridi, F., Fratini, E., Baglioni, P., 2011. Cement: a two thousand year old nano-colloid. J. Colloid Interface Sci. 357, 255–264.
Roosz, C., Gaboreau, S., Grangeon, S., Prêt, D., Montouillout, V., Maubec, N., Ory, S., Blanc, P., Vieillard, P., Henocq, P., 2016. Distribution of water in synthetic calcium silicate hydrates. Langmuir 32, 6794–6805.
Roosz, C., Grangeon, S., Blanc, P., Montouillout, V., Lothenbach, B., Henocq, P., Giffaut, E., Vieillard, P., Gaboreau, S., 2015. Crystal structure of magnesium silicate hydrates (M-S-H): the relation with 2:1 Mg–Si phyllosilicates. Cement Concr. Res. 73, 228–237.
Roosz, C., Vieillard, P., Blanc, P., Gaboreau, S., Gailhanou, H., Braithwaite, D., Montouillout, V., Denoyel, R., Henocq, P., Madé, B., 2018. Thermodynamic properties of C-S-H, C-A-S-H and M-S-H phases: results from direct measurements and predictive modelling. Appl. Geochem. 92, 140–156.
Sammartino, S., Siitari-Kauppi, M., Meunier, A., Sardini, P., Bouchet, A., Tevissen, E., 2002. An imaging method for the porosity of sedimentary rocks: adjustment of the PMMA method - example of a characterization of a calcareous shale. J. Sediment. Res. 72, 937–943.
Samper, J., Mon, A., Montenegro, L., Cuevas, J., Turrero, M.J., Naves, A., Fernández, R., Torres, E., 2018. Coupled THCM model of a heating and hydration concrete-bentonite column test. Appl. Geochem. 94, 67–81.
Suquet, H., Iiyama, J.T., Kodama, H., Pezerat, H., 1977. Synthesis and swelling properties of saponites with increasing layer charge. Clay Clay Miner. 25, 231–242.
Taylor, H.F.W., 1992. Cement Chemistry, second ed. (London).
Torres, E., Turrero, M.J., Garralón, A., Cuevas, J., Fernández, R., Ortega, A., Ruíz, A.I., 2019. Stable isotopes applied to the study of the concrete/bentonite interaction in the FEBEX in situ test. Appl. Geochem. 100, 432–443.
Tosca, N.J., Masterson, A.L., 2018. Chemical controls on incipient Mg-silicate crystallization at 25°C: implications for early and late diagenesis. Clay Miner. 49, 165–194.
Turrero, M.J., Cloet, V., 2017. In: Nagra (Ed.), FEBEX-DP Concrete Ageing, Concrete/bentonite and Concrete/rock Interaction Analysis. Wettingen, Switzerland, p. 5430, 282.
Turrero, M.J., Fernández, A.M., Peña, J., Sánchez, M.D., Wersin, P., Bossart, S.M., Melón, A., Garralón, A., Yllera, A., Gómez, P., Hernán, P., 2006. Pore water chemistry of a Paleogene continental mudrock in Spain and a Jurassic marine mudrock in Switzerland: sampling methods and geochemical interpretation. J. Iber. Geol. 32, 233–258.
Valkov, M., Simha, G., 2012. Vermiculite: Structural Properties and Examples of the Use.
Velde, B., 1985. Clays Minerals: A Physico-Chemical Explanation of Their Occurence. Elsevier, Amsterdam.
Vespa, M., Lothenbach, B., Dähn, R., Huthwelker, T., Wieland, E., 2018. Characterisation of magnesium silicate hydrate phases (M-S-H): a combined approach using synchrotron-based absorption-spectroscopy and ab initio calculations. Cement Concr. Res. 109, 175–183.
Villar, M.V., 2017. FEBEX-DP postmortem THM/THC analysis. In: 16-17, N.r.N., p. 142pp. Nagra report NAB 16-17.
Xie, M., Mayer, K.U., Claret, F., Alt-Epping, P., Jacques, D., Steefel, C., Chiaberge, C., Simunek, J., 2015. Implementation and evaluation of permeability-porosity and tortuosity-porosity relationships linked to mineral dissolution-precipitation. Comput. Geosci. 19, 655–671.